In: 2023 AIAA Aviation and Aeronautics Forum and Exposition (AIAA AVIATION Forum), 12-16 June 2023, San Diego, CA
DOI: 10.2514/6.2023-3467

Design considerations of non-axisymmetric exhausts for large civil aero-engines

J. Hueso-Rebassa* , D. MacManus† , I. Goulos‡ , F. Tejero§
Cranfield University, Cranfield, Bedfordshire, MK43 0 AL, United Kingdom

In order to reduce fuel consumption, the next generation of aero-engines are expected to operate with higher bypass ratios and lower fan pressure ratios. This will improve the propulsive efficiency of the power plant and reduce specific fuel consumption. Higher bypass ratios will be mostly accommodated with larger fan diameters. However, this will increase the size and mass of the powerplant, which could penalise the overall aircraft drag and erode some of the aero-engine cycle benefits. In addition, future configurations may require more close-coupled installations with the airframe due to structural and ground clearance requirements. This tendency may further exacerbate the adverse aerodynamic installation effects. A better integration of UHBR aero-engines with the airframe could be achieved with non-axisymmetric separate-jet exhausts. Non-axisymmetric configurations of the bypass nozzle can improve the performance of the aircraft by mitigating some of the penalising aerodynamic effects induced by the installation of the power plant. In this context, three-dimensional configurations of exhaust systems are parametrised and integrated with the propulsion system through a refined control of the geometry. The power plant is installed on the NASA Common Research Model and assessed with CFD. The design of non-axisymmetric exhausts is embedded in a relatively low-cost optimisation process. The method is based on response surface models and targets the optimisation of the aircraft net vehicle force for different design concepts of non-axisymmetric exhaust systems and several installation configuration. It is concluded that the optimisation of installed non-axisymmetric exhausts can benefit the overall aircraft net vehicle force between $0.5 - 0.9\%$ **of the engine nominal thrust, depending on the installation position.**

I. Introduction

Future civil aero-engines will operate with higher bypass-ratios (BPR) than current power-plants to improve propulsive efficiency and to reduce specific thrust [1]. This will be accompanied by an increase in fan diameter which could increase overall aircraft drag and thereby erode some of the aero-engine cycle benefits. Larger propulsion systems introduce an integration challenge. For podded under-wing configurations, Ultra-High Bypass Ratio (UHBR) aero-engines may require a close coupled installation with the wing to meet ground clearance requirements [2]. In such arrangements, the aerodynamic interference between propulsion system and airframe could penalise the aircraft Net Vehicle Force (NVF) relative to a more conventional installation position [3]. This is partly related to a reduction of the exhaust system performance [3]. For example, the Gross Propulsive Force (GPF) could be reduced by 3.5% of the engine nominal thrust relative to conventional installation positions [3]. For these reasons, it is useful to consider the effects of engine-aircraft integration in the early stages of the design of the propulsion system and airframe.

A. Non-axisymmetric exhausts for propulsion integration

An improved integration of UHBR engines with the airframe can be achieved with non-axisymmetric exhaust systems [4–6]. Non-axisymmetric configurations of the exhaust typically involve scarfed [4, 7] and non-circular designs of the bypass or core nozzles [4, 8]. Non-axisymmetric designs of the bypass nozzle can mitigate the aerodynamic effects induced by the installation of the powerplant [4, 6]. Therefore, these configurations could potentially enable a more close coupled integration of the propulsion system with the airframe. Otter et al. [4–6] investigated the aspects of propulsion system integration with conventional nacelles and non-axisymmetric separate-jet exhaust systems. An

*Research Fellow in Propulsion Aerodynamics, Centre for Propulsion and Thermal Power Engineering, Cranfield University, j.hueso-rebassa@cranfield.ac.uk
†Head of Gas Turbine Technology Group, Centre for Propulsion and Thermal Power Engineering, Cranfield University
‡Lecturer in Propulsion Integration, Centre for Propulsion and Thermal Power Engineering, Cranfield University
§Lecturer in Propulsion Systems Design, Centre for Propulsion and Thermal Power Engineering, Cranfield University

overall benefit in aircraft net vehicle force (NVF) of 0.8% relative to the baseline axisymmetric separate-jet exhaust was reported. This was achieved through non-axisymmetric perturbations of the bypass trailing edge that were controlled with intuitive Class-Shape Transformation functions (iCST) [9–11]. However, the research was limited to sensitivity studies of some of the exhaust design parameters and did not consider the optimisation of such configurations. A better understanding of the design space and aerodynamic effects that drive the performance of non-axisymmetric exhaust systems could enable further reductions of aircraft fuel burn. Therefore, there is a need to develop optimisation methods for non-axisymmetric exhausts that are coupled with compact state-of-art nacelles [12] and account for the effects of engine-aircraft integration.

B. Optimisation of separate-jet exhausts

The aerodynamic shape design and optimisation of exhaust systems is a complex non-linear problem where a substantial number of design variables are required to characterise exhaust geometries [5, 13, 14]. In addition, the numerical solution with Computational Fluid Dynamics (CFD) can involve notable computational costs. For these reasons, the use of conventional optimisation methods based on Reynolds Averaged Navier-Stokes (RANS) equations makes the computational cost prohibitive for the exploration and optimisation of large-dimensional design spaces. Therefore, lower-cost design methodologies are required. In this context, optimisation methods based on Response Surface Models (RSM) may offer computational benefits. RSM based optimisation alleviates the computational requirements of aerodynamic shape optimisation by defining a simplified mathematical relationship that approximates the response of the systems based on fewer numerical simulations [15]. Consequently, RSMs can be used to drive the optimisation algorithm without CFD evaluations in the process. Different design and optimisation methodologies of propulsion system configurations used RSMs. These include optimisation for preliminary engine design [16], optimisation of nacelle geometries [17–19] and the optimisation of separate-jet exhaust systems[13, 14, 20, 21].

Goulos et al. [20] developed an integrated design space exploration (DSE) and optimisation framework for two-dimensional axisymmetric separate-jet exhausts that were characterised with eleven independent geometric degrees of freedom (DOF). The methodology was based on the genetic algorithm (GA) optimisation of a Kriging RSM [22, 23] that was constructed from CFD generated aerodynamic data. The method optimised the Net Propulsive Force (NPF) of a conventional and an UHBR exhaust systems and achieved substantial benefits relative to the baseline configurations. A later investigation with the same methodology [21] optimised the overall velocity coefficient ($C_v^{Overall}$) of a similar exhaust system and reached benefits of 0.065% in $C_v^{Overall}$ and 0.3% in the bypass discharge coefficient (C_d^{BP}) relative to the baseline design. The same methodology was also applied to the optimisation of exhaust systems together with OGV total pressure (P_t) and total temperature (T_t) inflow profiles at the bypass duct inlet [14] and to the optimisation of bypass after-body geometries for Very High Bypass Ratio (VHBR) turbofans [13].

C. Optimisation of installed propulsion system configurations

The use of RSMs provides a way to characterise the design space and enables the global optimisation of the system with a reduced number of CFD evaluations. However, the computational time required by RANS CFD simulations limits the design capabilities. For installed configurations of propulsion systems, even the acquisition of enough data to build reliable surrogate models is infeasible within an industrial design context. The use of lower-fidelity CFD such as Euler methods may provide an approximation of the aerodynamics of installed propulsion systems at a fraction of the computational cost[24]. This allows wider and more thorough explorations of the design space and may enable the acquisition of sufficient reliable data to formulate prediction models.

Sanchez-Moreno et al.[25] developed a Kriging RSM based optimisation for installed configurations of non-axisymmetric compact nacelles. The design space was characterised with nine degrees of freedom and it was sampled with Euler CFD. Kriging RSMs were developed from the nacelle design database and were used in a GA optimisation. The final optimum design was assessed with RANS CFD. The optimisation method was able to identify nacelle designs that benefited the aircraft net vehicle force by $0.006F_N$, relative to the baseline configuration. This is approximately equivalent to a reduction in cruise fuel burn of 0.6%. The methodology reduced the computational cost by a factor of thirty-six relative to the equivalent optimisation with RANS CFD. This enabled the use of low-fidelity methods such as Euler CFD and RSM based optimisation for installed configurations of the propulsion system. However, this study did not consider the optimisation of the exhaust system.

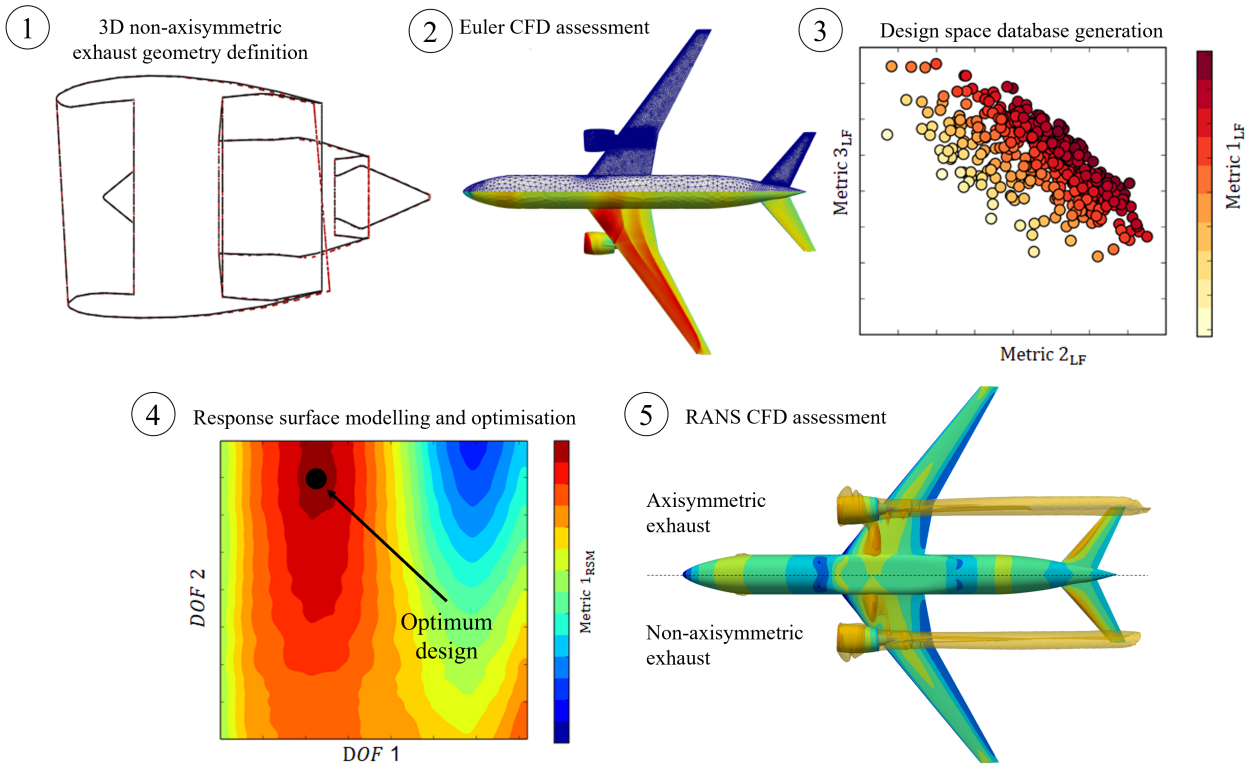

Fig. 1 Flow diagram of the low-fidelity design methodology for installed non-axisymmetric exhausts.

D. Scope of the present work

There is a need to design compact nacelles and non-axisymmetric exhaust systems to maximise the installed benefits of novel UHBR aero-engines. It is envisaged that a reduction in fuel burn may be achieved for power-plant installations which feature a non-axisymmetric nacelle and non-axisymmetric separate-jet exhaust system. Whilst there have been previous investigations on the design and optimisation of installed non-axisymmetric nacelles[25, 26], there is very limited research on the design optimisation of non-axisymmetric exhausts. This work develops a relatively low-cost design methodology for non-axisymmetric separate-jet exhaust based on RSM driven optimisation to improve the overall aircraft and engine performance. The aim is to quantify the potential aerodynamic benefits of non-axisymmetric exhaust systems optimised for different engine installation positions and with different non-axisymmetric configurations of the bypass nozzle exit area and after-body.

II. Methodology

The design of non-axisymmetric exhausts for installed configurations comprises all the steps of aerodynamic shape design and optimisation (Fig. 1). These include the parametrisation of three-dimensional exhaust geometries, the installation of the propulsion system with the airframe and the computational assessment of the complete engine-airframe system. The design methodology starts with a design of experiment (DOE) where the design space of non-axisymmetric exhausts is sampled to compile a database of designs. All designs in the database are assessed with Euler CFD and the aerodynamic metrics of interest are calculated. With the resultant data, Response Surface Models (RSMs) are formulated. RSMs are statistical models that can approximate the response of a complex non-linear system for a target set of inputs. The RSMs are employed as surrogate models of the system in an optimisation process. As the optimisation is performed on the RSMs, no CFD evaluation is involved during the optimisation. Finally, the optimum design is evaluated with RANS CFD.

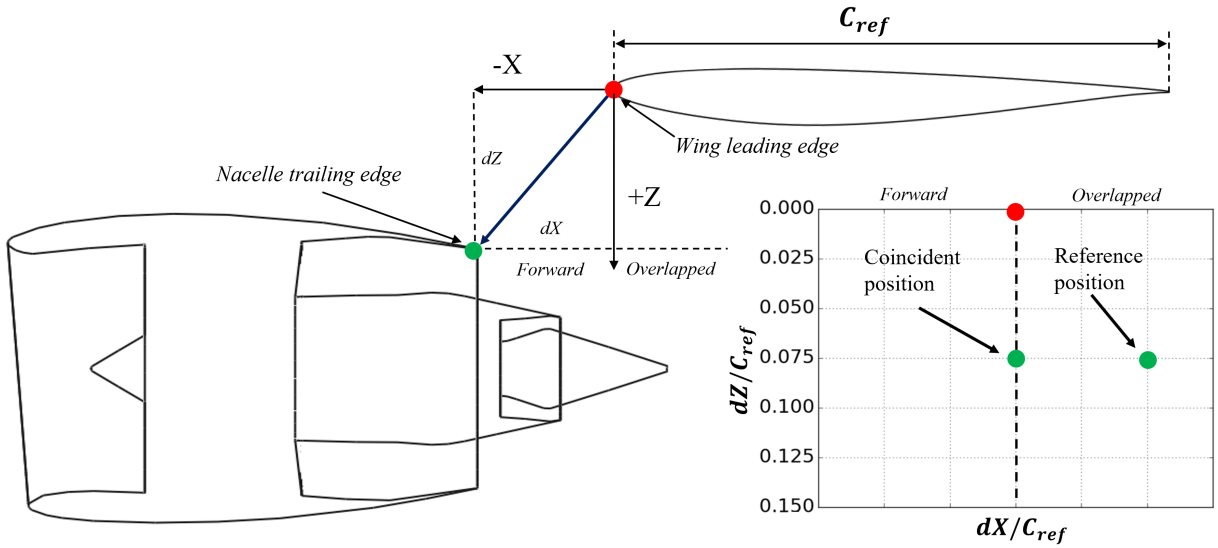

Fig. 2 Schematics of the installation positions considered in this section.

A. Propulsion system and installation

The baseline propulsion system is a modern Ultra-High Bypass Ratio Engine (UHBR) with bypass ratio of $BPR = \dot{m}^{BP}/\dot{m}^{CR} > 15$ [3] and a standard nominal thrust of 60kN ($F_N \approx 60kN$) [3]. The reference propulsion system is configured with an axisymmetric separate jet exhaust that was optimised by Goulos et al.[20] in a two-dimensional, axisymmetric framework. The nacelle is compact and non-axisymmetric with droop and scarf at the intake to improve its performance at incidence conditions [12, 18]. It was optimised by Tejero et al. [18, 27] using an uninstalled, three-dimensional methodology.

The propulsion system is installed under wing of the NASA Common Research Model (CRM) [28–30] with a pylon. The installation pitch ($\phi_{ptich} = 1.75^o$) and toe ($\phi_{toe} = 2.25^o$) angles of the propulsion system are based on the reference values of the CRM with a through-flow nacelle [31]. The installation position is defined at a fixed span-wise location as the offset between the leading edge of the wing and the trailing edge of the fan cowl at its top line (Fig. 2). The horizontal (dX/C_{ref}) and vertical (dZ/C_{ref}) components of the position are normalised by the wing chord ($C_{ref} = 7.8m$ [30]) of the local airfoil at the target span-wise location. In a non-axisymmetric exhaust configuration the axial position of the fan cowl trailing edge may vary azimuthally relative to the axisymmetric baseline. For this reason, the installation position is always referred to the axisymmetric equivalent configuration. In this work, two installation positions are studied. These are an overlapped configuration of the nacelle with the wing and a coincident installation position (Fig. 2). These are in the range of close coupled positions considered in previous studies [3].

The operating conditions of the baseline configuration are representative of the mid-cruise segment of a long range flight. The cruise altitude is $h = 10668m$, with a flight Mach number of $M_\infty = 0.85$ and a Reynolds number based on the CRM reference chord of $Re_{C_{ref}} = 46 \times 10^6$. The ambient conditions of static pressure (p_∞) static temperature (t_∞) and density (ρ_∞) are calculated with the International Standard Atmosphere (ISA) model[32]. The engine cycle is based on published information[3]. Cycle data of Overall Pressure Ratio (OPR) and Turbine Entry Temperature (TET) were used by Goulos et al. [3, 33] to derive values for Fan Nozzle Pressure Ratio (FNPR) and Core Nozzle Pressure Ratio (CNPR) on the basis of minimising Specific Fuel Consumption (SFC) at mid-cruise conditions. The values used for the mid-cruise operation are $FNPR = P^{BP}_{inlet}/p_\infty \approx 2.2$ and $CNPR = P^{CR}_{inlet}/p_\infty \approx 1.5$ [3].

B. Parametrisation of non-axisymmetric exhaust system geometries

The parametrisation of non-axisymmetric exhaust systems is achieved with perturbations of the bypass trailing edge relative to the baseline axisymmetric geometry. The methods for the generation of non-axisymmetric exhaust geometries are based on intuitive Class Shape Transformation functions (iCST) [4–6]. The perturbations are imposed with azimuthal iCSTs that modify the constrained points of each aero-line. In a cylindrical reference frame centred on the exhaust, azimuthal positions from $\psi = 0^o$ to 180° correspond to the outboard side of the propulsion system while

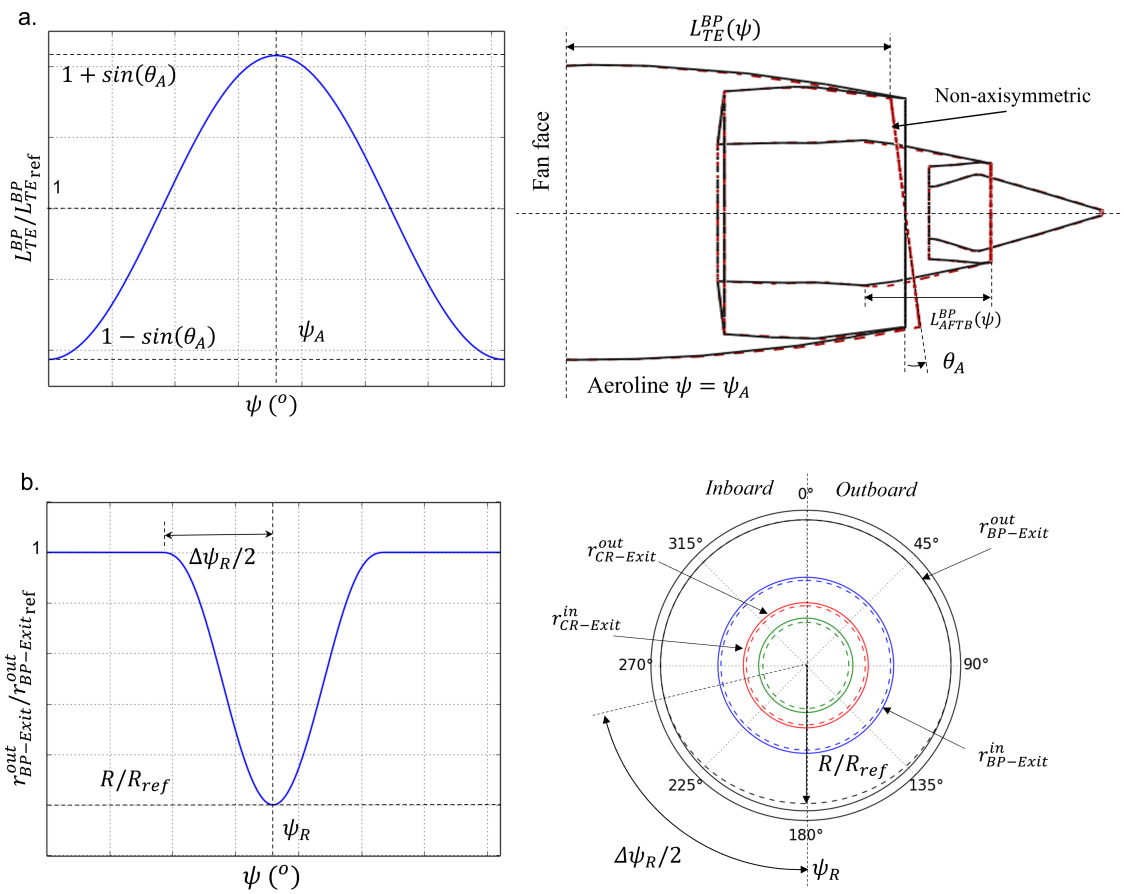

Fig. 3 Azimuthal perturbations of the bypass trailing edge. (a) Perturbation of the axial position and (b) perturbation of the trailing edge radius.

positions from $\psi = 180^o$ to 360° refer to the inboard-side. The present work focuses on perturbations that modify the bypass trailing edge radius and axial position as a function of the azimuth (ψ). Two independent types of perturbations are considered. These involve axial and radial perturbations of the bypass trailing edge. Both families of perturbations are combined into a multi-dimensional design space.

The axial perturbation, also called shear[34], is a particular case of nozzle scarfing [4, 7] where only the axial component of the transformation is considered. The shear perturbation varies the axial location of the bypass trailing edge azimuthally ($L_{TE}^{BP} = f(\psi)$) (Fig. 3a). The perturbation can be applied at any azimuthal location of the exhaust system and is characterised by two degrees of freedom, ψ_A and θ_A. The first parameter (ψ_A) sets the azimuthal position where the axial offset of the trailing edge is maximum. This definition is equivalent to the specification of the rotation axis. The second design parameter is the shear angle (θ_A) and it relates to the magnitude of the perturbation.

The second type of perturbation is an azimuthal distribution of the radius of the bypass trailing edge ($r_{out-exit}^{BP}$, Fig. 3b) [6]. It consists of azimuthal iCSTs that allow localised changes of the bypass trailing edge radius. The perturbation is controlled by three design parameters: ψ_R, R/R_{ref} and $\Delta\psi_R$. ψ_R is the azimuthal position where the perturbation is centred, R/R_{ref} is the radius ratio relative to the axisymmetric reference exhaust and $\Delta\psi_R$ corresponds to the azimuthal extend where the perturbation is effective.

1. Design of the bypass exhaust exit area

The perturbations of the bypass trailing edge introduce a challenge for the design of the bypass nozzle. The bypass exit annulus can no longer remain axisymmetric. As the bypass trailing edge radius is reduced at a target ψ_R with a $\Delta\psi_R$, the inner aerolines of the exhaust need to be adjusted to guarantee the target nozzle exit area. Two different methods are developed and investigated to maintain the target bypass exit area. The first method sets a circumferentially

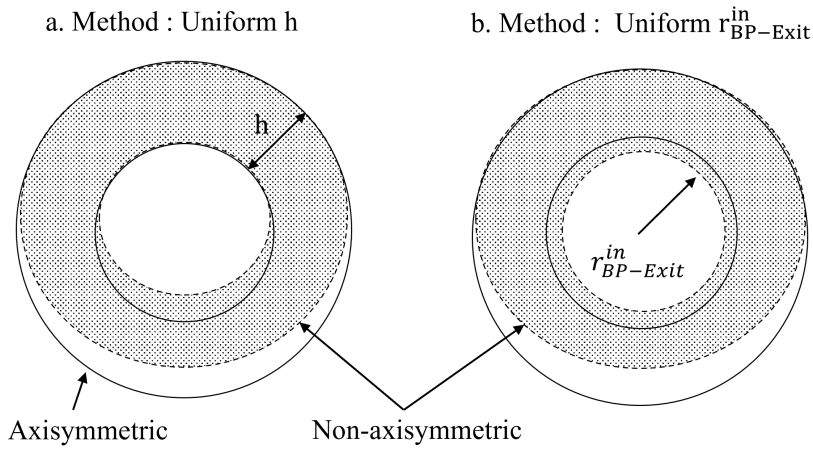

Fig. 4 Schematics of the two bypass area control methods. (a) Uniform h method and (b) uniform $r^{in}_{BP-Exit}$.

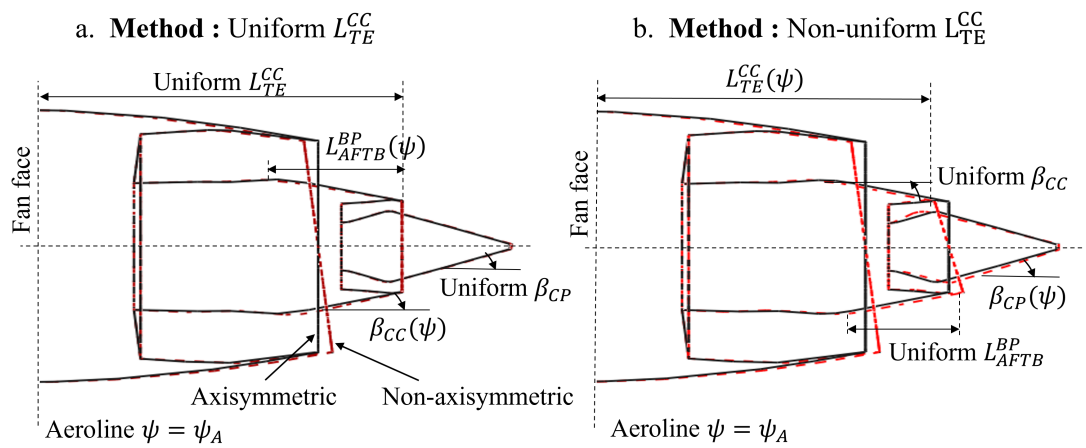

Fig. 5 Schematics of the two after-body control methods. (a) Uniform L^{cc}_{TE} and (b) non-uniform L^{cc}_{TE}.

invariant bypass exit nozzle height (uniform h) (Fig. 4a). The method reduces the inner radius of the bypass exit plane ($r^{BP}_{BP-Exit}$) consistently with the perturbation. The nozzle height (h) is kept constant along the azimuthal extent and results into non-circular core cowl shapes. The second method maintains a circumferentially invariant bypass exit inner radius (uniform $r^{in}_{BP-Exit}$, Fig. 4b). The uniform $r^{in}_{BP-Exit}$ method preserves the circular shape of the inner annulus of the bypass nozzle and adjusts the exit area with a uniform reduction of $r^{in}_{BP-Exit}$. Note that the core nozzle outer and inner annuli are also reduced as a consequence.

2. After-body design

The bypass after-body also needs to be adjusted. Although the shear perturbation is applied on the bypass trailing edge, the variation of the bypass exhaust length at the outer aerolines propagates to the inner aerolines and after-body. At a single azimuthal position, the inner point of the bypass exit plane is similarly displaced axially. Two methods to control the after-body have been developed and investigated for non-axisymmetric bypass geometries. The methods depend upon which of the after-body parameters are preserved. The two possible options include after-bodies with uniform axial position of the core cowl trailing edge (uniform L^{cc}_{TE}) or sheared after-bodies (non-uniform L^{TE}_{cc}) (Fig. 5). Both methodologies inevitably produce non-axisymmetric after-bodies.

The uniform L^{TE}_{cc} method keeps the core cowl trailing edge at a constant axial position across the azimuthal span (Fig. 5a). However, as the position of the bypass exit plane changes azimuthally, the core cowl boat tail angle (β_{cc}) and the bypass after-body length (L^{BP}_{AFTB}) are also varied. The second method (non-uniform L^{TE}_{cc}) maintains a uniform β_{cc} and

L^{BP}_{AFTB} across the azimuthal span and produces sheared core cowls (Fig. 5b). Note that the non-uniform L^{TE}_{cc} method also results in non-axisymmetric core nozzles. Sheared core cowls modify the length of core duct asymmetrically. In these cases, the core nozzle is handled similarly to the uniform L^{TE}_{cc} method where the plug trailing edge is kept at a uniform position. This leads to a non-uniform distribution of the core plug half-cone angle (β_{cp}, Fig. 5b).

Both after-body methods are controlled with the non-dimensional mean after-body length ($\overline{L^{BP}_{AFTB}/L^{BP}_{AFTB_{ref}}}$). The mean after-body length is calculated as the azimuthal average. The definition of such a parameter enables the variation of the core cowl length consistently between both methods. On the first method (uniform L^{TE}_{cc}) the parameter directly sets the axial position of the trailing edge while for the second method (non-uniform L^{TE}_{cc}) the parameter enforces a mean axial position of the core cowl trailing edge upon which the shear is applied. For simplicity, the mean after-body length is expressed as $L^{BP}_{AFTB}/L^{BP}_{AFTB_{ref}}$.

3. Computational assessment

Computational fluid dynamics (CFD) methods of different fidelities are used to assess the exhaust systems. These comprise compressible Euler methods as the lower-fidelity function and compressible Reynolds Averaged Navier Stokes (RANS) as the higher-fidelity method. The RANS solution method is based on a density-based, implicit and steady-state CFD solver [35]. It is coupled with 2nd order convective schemes and the $k-\omega$ SST turbulence model [36]. The dynamic viscosity of the fluid is calculated with the Sutherland's law [37] for both CFD methods.

The boundary conditions are set according to the operating conditions of the aircraft and propulsion system. The fan face is treated as mass flow pressure outlet that enforces a desired mass flow capture ratio (MFCR). Both nozzle inlets are modelled as total pressure inlets with the values specified according to their fan (FNPR) and core (CNPR) pressure ratios and total temperatures, respectively. The inflow conditions are set as pressure far field with $M_\infty = 0.85$ and a symmetry plane is used.

The meshes for the RANS CFD method are unstructured, with layers of triangular prisms in the boundary layer region and tetrahedra elsewhere. The grid is refined with volumetric density boxes on the regions of interest (jet, wing, pylon, ducts,..). This approach ensures a $y^+ < 1$ over the whole geometry and results in 115×10^6 cells.

The computational methodology was validated against the experimental data of dual stream flow reference nozzle (DSFRN) for the exhaust performance [38] and against the CRM for drag prediction[28, 30][3]. For the DSFRN, a root mean squared error between CFD and measurements of 0.033% was obtained for the velocity coefficient across the FNPR range (1.4 to 2.8). For the CRM at cruise, the airframe drag coefficient was calculated within 13 drag counts of the measured values for the clean and through flow nacelle configurations

4. Thrust and drag accounting system

A modified near-field method for thrust and drag bookkeeping [39] is applied to extract the metrics of interest. The method was expanded to installed aero-engine configurations and it is detailed in the work of Goulos et al. [3]. Therefore, only a summary is included. For installed configurations and non-axisymmetric exhausts a 3D vectorial notation in the aerodynamic reference frame ($\hat{i}_D, \hat{i}_S, \hat{i}_L$) is considered. All the forces are composed by drag (D), lift (L) and side (S) terms. The forces that act on the propulsion system and airframe are represented in figure 6. The aerodynamic forces applied by the flow on the surfaces and stream tube boundaries are denoted by ϕ and θ. the forces are evaluated through numerical integration of gauge static pressure ($p - p_\infty$) and shear-stresses (τ) along the surfaces. The thrust domain includes all the forces inside the intake and exhaust stream tubes, while the drag domain includes the forces outside of the stream tubes (Fig. 6). The wall forces in the drag domain are defined as ϕ while in the thrust domain are θ. Gauge stream forces (F_G) and mass flows ($\dot{m}$) are also calculated with numerical integration over the fan face (2), bypass (13) and core (7) inlet boundaries (Fig. 6). F_G are computed with the stream and static pressure forces.

The modified Gross Propulsive Force (GPF^*) (Eq. 1) considers the gauge forces at both nozzles exit planes and wall forces within the thrust domain. The modified nacelle drag (D^*_{nac}) (Eq. 2) accounts for the pre-entry force (ϕ_{pre}) and forces that act on the fan cowl (ϕ_{cowl}) and on the drag domain of the pylon (ϕ_{pyl}). The airframe drag ($D_{A/F}$) includes the wall forces over the wing, fuselage and tail. The aircraft drag ($D_{A/C}$) combines the drag contributions of the airframe and nacelle (Eq. 3). The intake momentum (F_{G0}) (Eq. 4) comprises the intake mass flow ($\dot{m}_{fan}$) and the free-stream velocity (v_∞). The performance of complete propulsion system-airframe configurations is reported in this study in terms of Net Vehicle Force (NVF) (Eq. 5).

$$(GPF^*)_D = (F_{G_{13}} + F_{G_7})_D - (\theta_{BP} + \theta_{CR} + \theta_{CC} + \theta_{plug} + \theta_{pyl})_D \tag{1}$$

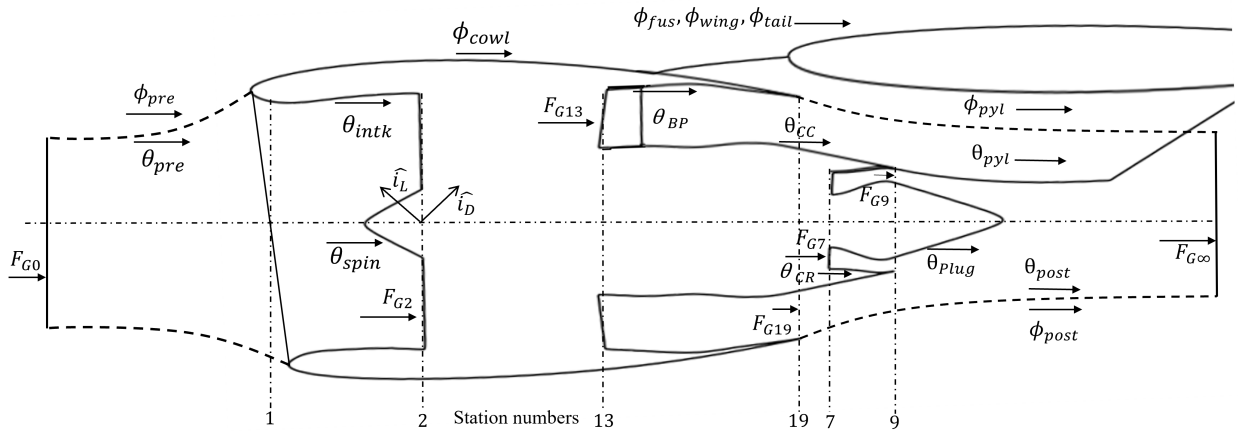

Fig. 6 Schematics of the thrust and drag accounting method.

$$D^*_{nac} = \left(\phi_{pre} + \phi_{cowl} + \phi_{pyl}\right)_D \tag{2}$$

$$D_{A/C} = D^*_{nac} + D_{A/F} \tag{3}$$

$$F_{G0} = \dot{m}_{fan} v_\infty \tag{4}$$

$$NVF = (GPF^*)_D - F_{G0} - D^*_{nac} - D_{A/F} \tag{5}$$

All the metrics are for the CRM mid-cruise conditions with $C_L^{A/C} = 0.5$ (Eq. 6). The aircraft lift coefficient is computed with the lift components of the GPF^*, nacelle and airframe forces, normalized by the free-stream dynamic pressure (q_∞) and a wing reference area (A_{ref}).

$$C_L^{A/C} = \frac{(GPF^*)_L + L_{A/F} + L^*_{nac}}{q_\infty A_{ref}} \tag{6}$$

To evaluate the performance changes between two configurations, it is more convenient to express the metrics as variations relative to a reference configurations. The change in force metrics (ΔF) between non-axisymmetric (F_2) and axisymmetric (F_1) configurations are defined as the difference between the metrics normalised by the standard nominal thrust ($F_N = 60kN$[3]) and expressed as percent (Eq. 7). ΔF is positive for a performance benefit.

$$\Delta F = \frac{F_2 - F_1}{F_N} (\%) \tag{7}$$

For non-axisymmetric exhausts, the intake momentum remains constant relative to the baseline axisymmetric exhaust configuration. Consequently, the increment of NVF (ΔNVF) is the sum of the increments in modified gross propulsive force and aircraft drag (Eq. 8)

$$\Delta NVF = (\Delta GPF^*)_D + \Delta D_{A/C} \tag{8}$$

C. Response surface model based optimisation

The optimisation of installed non-axisymmetric exhausts is achieved through an RSM based methodology. First, the Latin Hypercube Sampling (LHS) method is used to generate the design databases [40]. The design databases are assessed with Euler CFD, which enables a wide exploration of the design space at a computational cost that is reduced by a factor of thirty-six relative to the equivalent optimisation using RANS CFD [25]. The aerodynamic data

of all the designs are used to formulate Kriging RSM [22, 23] which are used as surrogate models to drive a Genetic Algorithm optimisation (GA). The RSMs hyper-parameters of nugget size, correlation function and regression model were optimised for the best response of the model. The optimisation is based on a global single-objective genetic algorithm [41] and is configured with 100 generations, an initial population of 50 times the number of design parameters and a population size per generation of 25 times the number of DOF. These settings were tuned to ensure the convergence of the optimisation. Once the optimisation algorithm has identified an optimum non-axisymmetric exhaust, the design is assessed with RANS CFD.

The process targets the maximisation of the net vehicle force of non-axisymmetric exhausts relative to a baseline axisymmetric configuration (ΔNVF) while ensuring both the bypass and core discharge coefficients are maintained within certain limits.

III. Results and discussion

A. Definition of the design space and non-axisysmmetric exhaust databases

The design space of non-axisymmetric exhausts is characterised by six degrees of freedom (DoF). These are the two design variables that control the shear perturbation (ψ_A, θ_A), the mean after-body length ($L^{BP}_{AFTB}/L^{BP}_{AFTB_{ref}}$), and the three parameters of the perturbation of the bypass trailing edge radius (ψ_R, R/R_{ref}, $\Delta\psi_R$). The azimuthal positions of both perturbations (ψ_A, ψ_R) are bounded to cover all the azimuthal extend of the bypass nozzle ($0^o < \psi_{A,R} < 360^o$). The bounds of shear angle (θ_A) are inspired by previous nozzle scarfing studies[4]. The bypass trailing edge radius can be reduced by a maximum of 5% of the reference value (R/R_{ref} = 0.95 to 1) at ψ_R with an extend $\Delta\psi_R$. The bounds of the perturbation of radius (R/R_{ref}, $\Delta\psi_R$) are also inspired by previous studies[4, 6]. Finally, the maximum and minimum values of the mean after-body length ($L^{BP}_{AFTB}/L^{BP}_{AFTB_{ref}}$) are selected according to the values used in optimisation studies of two-dimensional axisymmetric exhausts[21].

The design space is sampled with a ratio of 80 samples per degree of freedom similar to other optimisations of installed propulsion systems [25]. This results in 480 exhaust designs spread across the design space. A total of four different datasets are generated using the same design parameters, bounds and sampling ratios (Table. 1). The difference between datasets are the design installation position (Fig. 2), bypass exit area (Fig. 4) and the after-body control methods (Fig. 5). Dataset DS1 targets the design of non-axisymmetric exhausts at the overlapped installation position (dX/C_{ref} = 0.03, dZ/C_{ref} = 0.075). The bypass exit area is designed with a uniform inner radius (uniform r^{in-BP}_{Exit}) and the after-body with a uniform L^{cc}_{TE} (Fig. 7a). The other datasets are created to study design variations related to changes of installation position (DS2), bypass after-body (DS3, Fig. 7b) and bypass area (DS4, Fig. 7c) definitions (Table 1).

Table 1 Summary of the non-axisymmetric exhaust datasets.

Dataset	dX/C_{ref}	dX/C_{ref}	BP Area	After-body	Design variables	Samples
DS1	0.03	0.075	uniform $r^{in}_{BP-Exit}$	uniform L^{cc}_{TE}	6	480
DS2	0.00	0.075	uniform $r^{in}_{BP-Exit}$	uniform L^{cc}_{TE}	6	480
DS3	0.03	0.075	uniform $r^{in}_{BP-Exit}$	non-uniform L^{cc}_{TE}	6	480
DS4	0.03	0.075	uniform h	uniform L^{cc}_{TE}	6	480

B. Verification of response surface models

The datasets are used to construct response surface models. The verification the RSMs constructed with Euler CFD data was based on the leave-one-out (LOO) cross validation methodology [42]. In this process, different RSMs (RMS_{LOO}) are created to predict the performance of each of the samples in the database. The data used to train each RSM includes all the data points in the database except the left-out sample to be predicted. The RSM predictions are finally correlated with the original CFD results in terms of linear regression and root mean squared deviation (RMSD, Eq. 9).

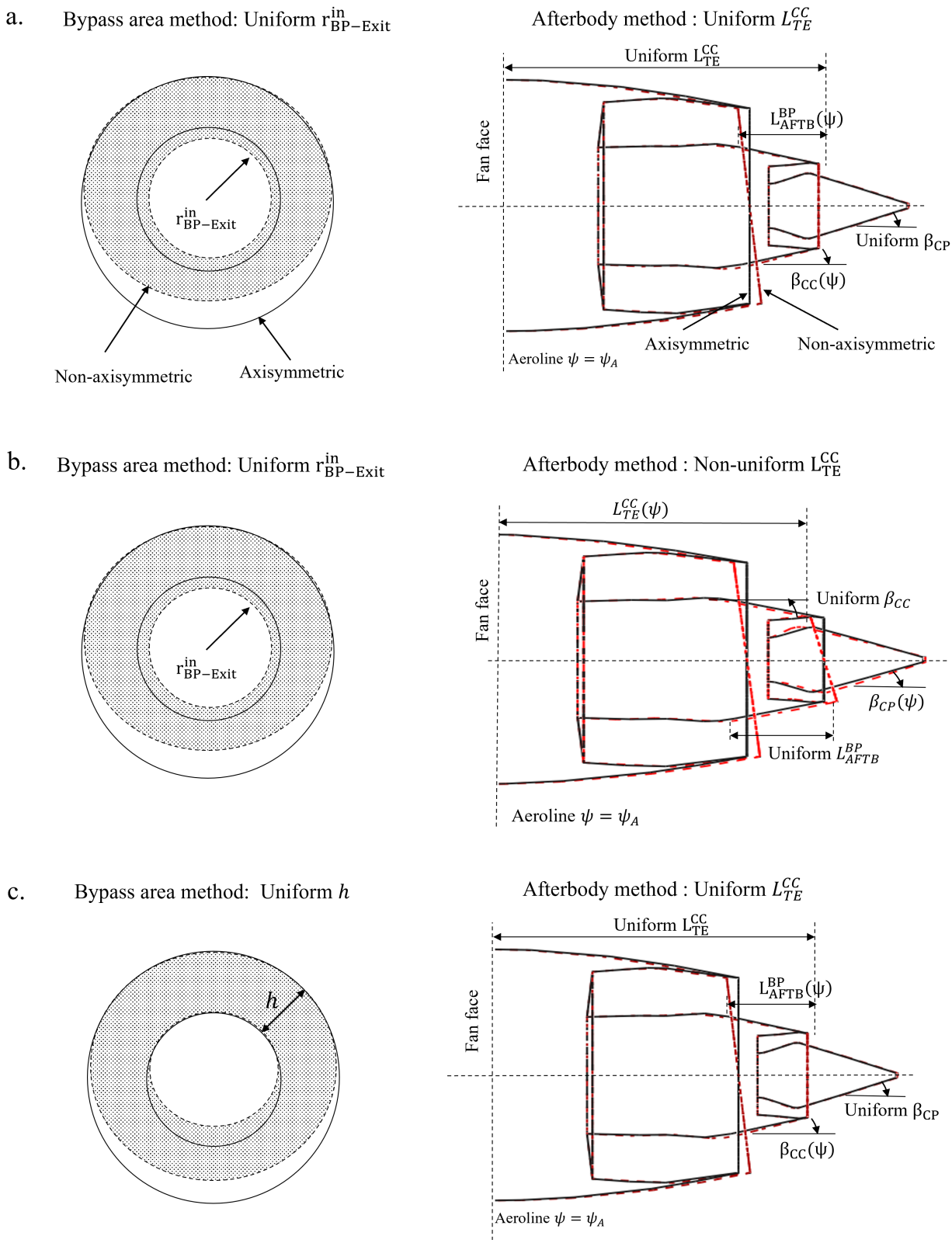

Fig. 7 Bypass exit area and after-body control for (a) databases DS1 and DS2, (b) DS3 and (c) DS4.

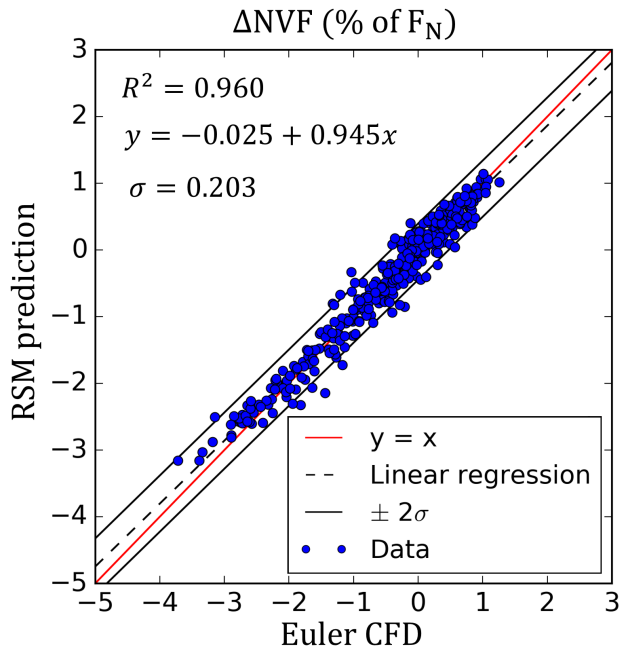

Fig. 8 Comparison of RSM predictions with Euler CFD results (Database DS1).

$$RMSD_{LOO} = \sqrt{\frac{1}{n}\sum_{i=1}^{n}\left(f(x_i) - RSM_{LOO}(x_i)\right)^2} \tag{9}$$

For the response surface model created with dataset DS1, the ΔNVF (Fig. 8 and Table 2) was predicted with a $R^2 = 0.96$, slope of 0.945 and a root mean squared deviation of $RMSD = 0.002F_N$, relative to the Euler CFD data. The same analysis was performed for the rest of the RSMs constructed with DS2, DS3 and DS4 (Table 2). In conclusion, the RMSD of ΔNVF for all RSMs was below $0.0023F_N$ and the coefficients of determination were greater than 0.938. For these reasons, the predictive capability of the RSMs was considered sufficient to be used in the optimisation studies.

Table 2 Results of the leave-one-out cross validation study for the RSMs of the different datasets.

Dataset	Metric	R^2	Intercept	Slope	RMSD
DS1	ΔNVF	0.960	-0.025	0.945	$0.0020F_N$
DS2	ΔNVF	0.938	-0.017	0.925	$0.0016F_N$
DS3	ΔNVF	0.953	-0.026	0.940	$0.0019F_N$
DS4	ΔNVF	0.952	-0.031	0.936	$0.0023F_N$

C. Optimisation of installed non-axisymmetric exhausts

The optimum non-axisymmetric exhaust design for maximum ΔNVF at an overlapped installation position with uniform $r^{in}_{BP-Exit}$ bypass area and uniform L^{cc}_{TE} after-body (design DS1-1) has an improvement in the overall aircraft performance of $\Delta NVF = 0.0067F_N$ when assessed with RANS CFD. Non-axisymmetric exhaust systems can improve the aircraft performance substantially, even when designed with a low-cost methodology based on Euler equations. The improvement of NVF relative to the baseline arises from a benefit in propulsive force ($(\Delta GPF^*)_D = 0.0098F_N$) and a penalty in aircraft drag ($\Delta D_{A/C} = -0.0031F_N$). The overall aircraft drag is the result of a benefit of nacelle drag ($\Delta D^*_{nac} = 0.031F_N$) that is countered by the airframe component ($\Delta D_{A/F} = -0.034F_N$). Opposite effects in propulsive

a. Schematic of the shear perturbation of the bypass trailing edge (DS1-1)

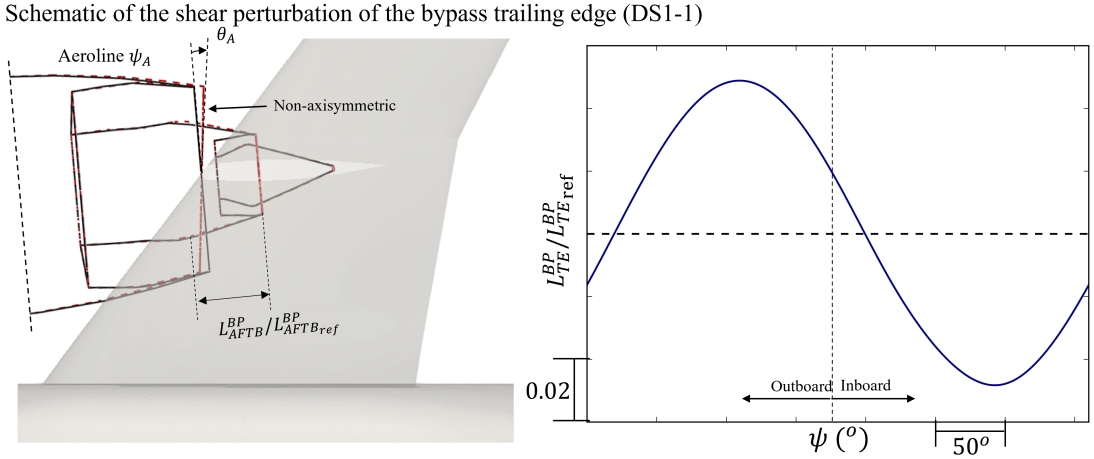

b. Schematic of the perturbation of the bypass trailing edge radius (DS1-1)

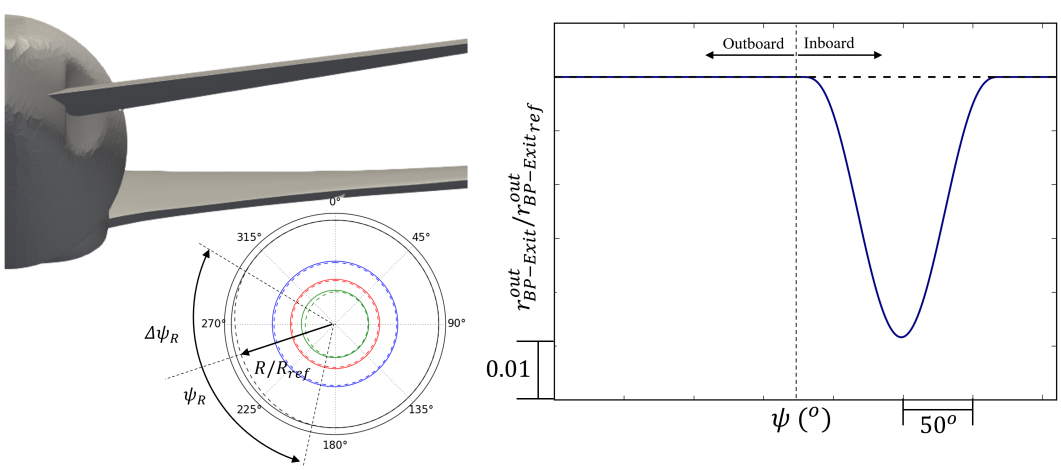

Fig. 9 Schematics of (a) shear and (b) radius perturbations of the bypass trailing edge of the optimum design (DS1-1).

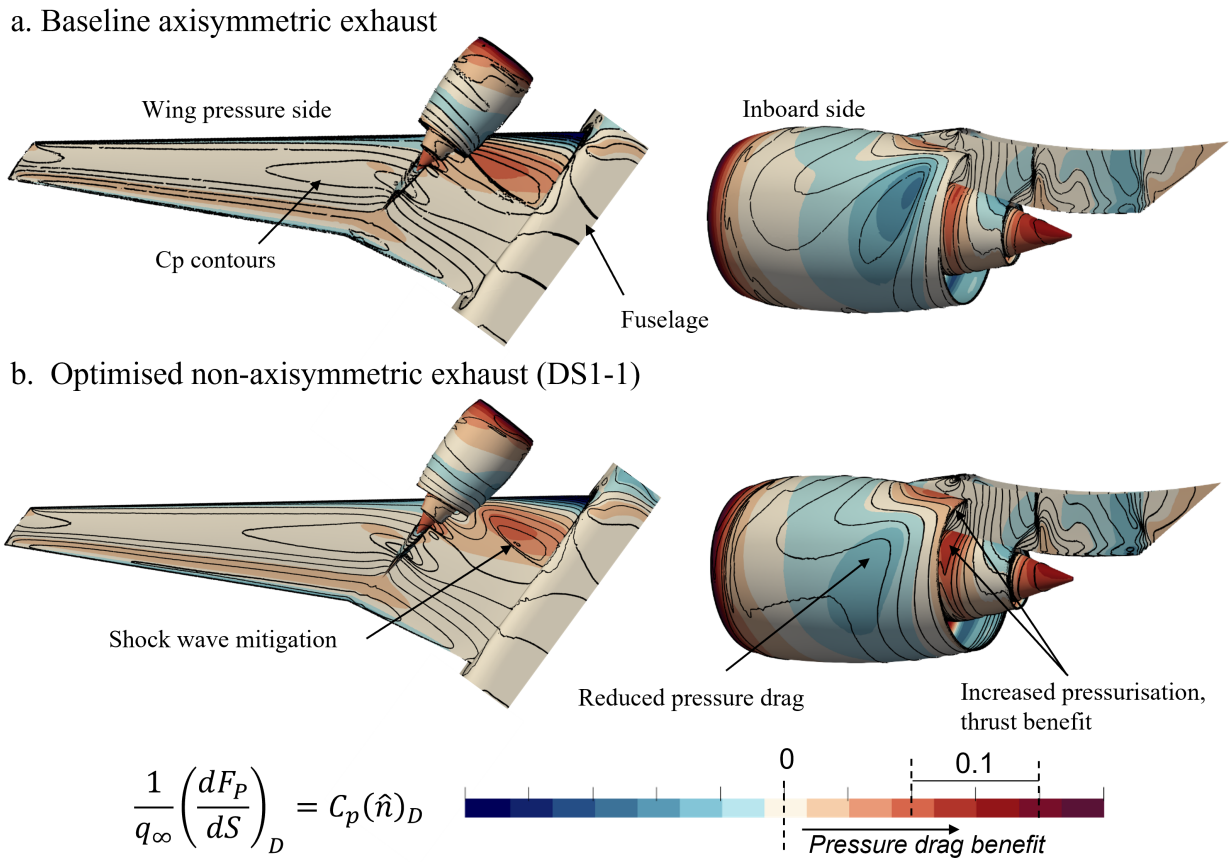

Fig. 10 Pressure drag distributions ($C_p(\hat{n})_D$) over the wing pressure side (left) and propulsion system inboard side (right) of the (a) axisymmetric baseline and (b) design DS1-1.

force and aircraft drag highlight the coupled nature of the system. Therefore, an installed design methodology for the propulsion system is required.

In terms of the non-axisymmetric perturbations of the bypass trailing edge, DS1-1 is configured with an inboard-sheared fan cowl and a reduced bypass trailing edge radius at the inboard-side (Fig. 9). The resultant non-axisymmetric design reduces the overlapping between nacelle and wing at the inboard side. This mitigates the shock-wave that forms between nacelle pylon and fuselage and weakens the pre-shock expansion (Fig. 10). This aerodynamic mechanism improves the gross propulsive force as a result of a better alignment of the thrust vector with the drag axis [43] and alters the pressure force distribution over the wing pressure side and nacelle.

D. Effect of the installation position on the design of non-axisymmetric exhausts

To evaluate the effect of the installation position on the design of the exhaust system, a second optimisation is carried out with the RSM constructed from DS2 (Table 2). DS2 is exactly the same as DS1 where the only difference being the design installation position. DS2 is assessed at a coincident installation (Fig. 2). The optimum non-axisymmetric exhaust systems for a coincident installation position (design DS2-1) improves the net vehicle force by $\Delta NVF = 0.0058F_N$ relative to the baseline axisymmetric exhaust system in the same position. This is approximately $0.001F_N$ less than the exhaust optimised for the overlapped position (DS1-1). Therefore, it can be concluded that non-axisymmetric exhausts could improve the aircraft performance for more benign installation positions. The split of ΔNVF into the force components (Fig. 11a) indicates the same general trends as in the overlapped position (DS1-1). However, the contribution of each component has changed. For a coincident installation position (DS2-1), $(\Delta GPF^*)_D$ is greater than DS1-1 but $D_{A/C}$ is increased. Compared with DS1-1, the relative increase in $D_{A/C}$ is mainly associated with the modified nacelle drag term.

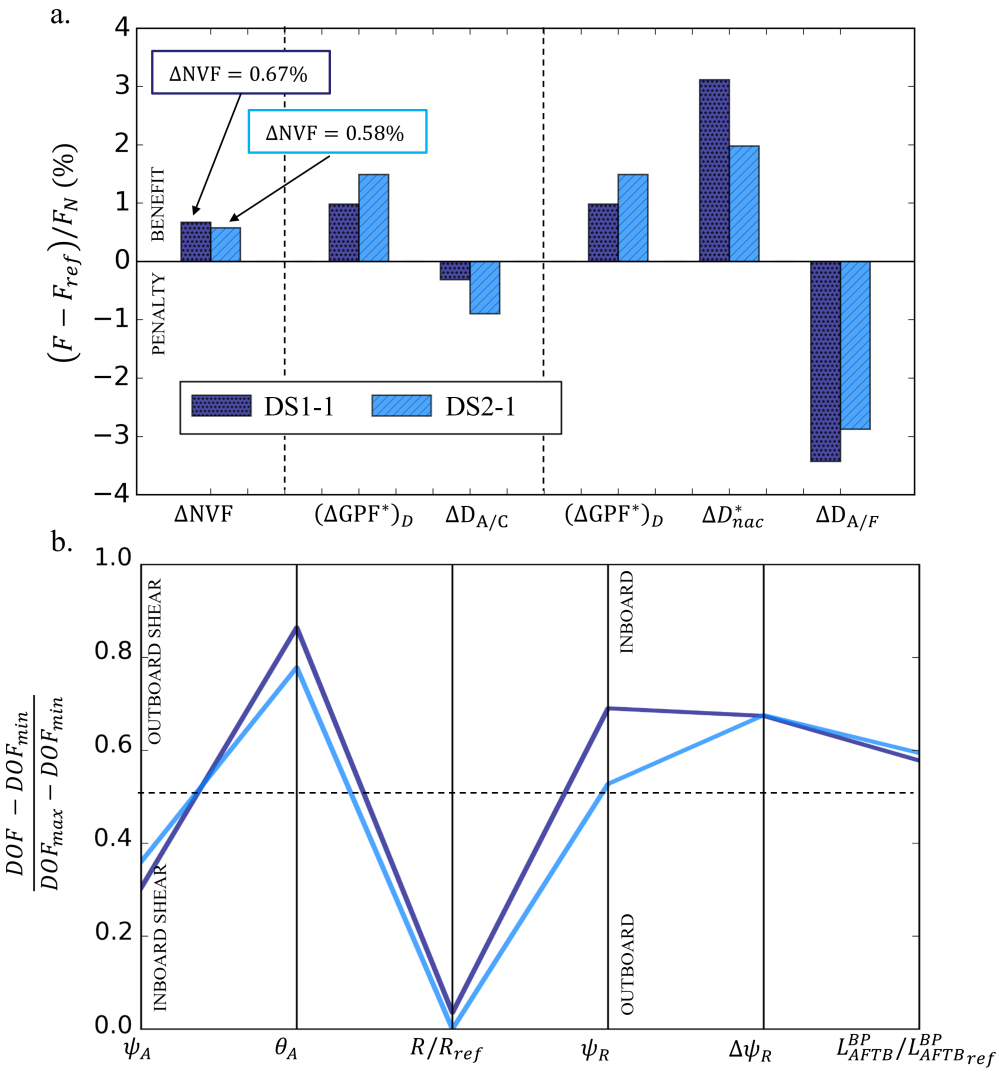

Fig. 11 (a) General decomposition of the net vehicle force benefit and (b) parallel coordinates chart of designs DS1-1 and DS2-1. Forces are expressed as increments (Δ) relative to the baseline configuration where a positive value implies a beneficial effect. All results are based on RANS CFD assessments.

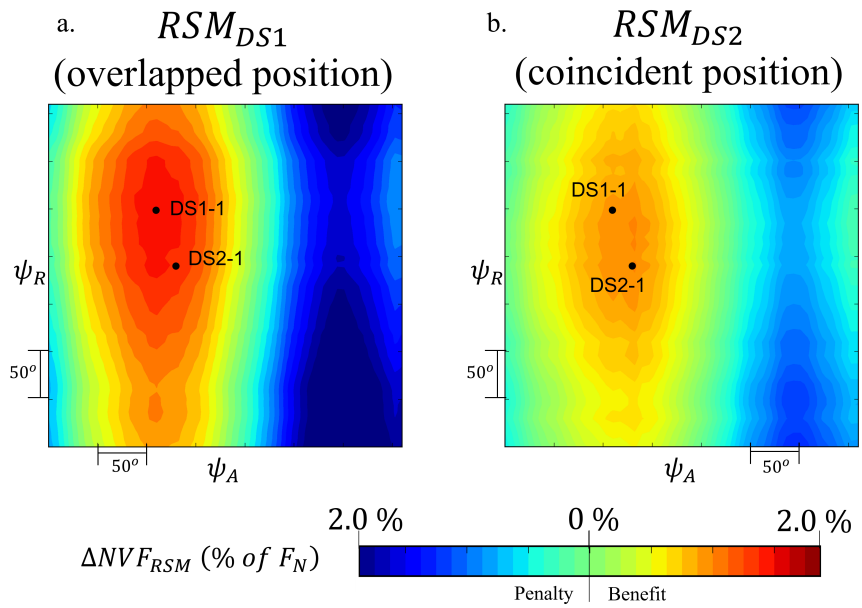

Fig. 12 Design sensitivities of ΔNVF with ψ_A and ψ_R for the RSMs constructed with datasets (a) DS1 (overlapped installation position) and (b) DS2 (coincident installation position).

In terms of design parameters, the optimum design at the coincident position (DS2-1) is also configured with inboard shear (Fig. 11b). However, the location of the perturbation is at greater values of ψ_A relative to DS1-1. The azimuthal position of the perturbation of bypass trailing edge radius (ψ_R) has also been displaced towards $\psi = 180^o$. These results demonstrate that the optimum ΔNVF region of the design space is altered with the installation position. The RSMs are interrogated around the optimum designs to illustrate how the distribution of ΔNVF with the design variables is affected by the installation position (Fig. 12). In this analysis, all the design variables are fixed to their optimum values except for the interrogated variables. In the figure, the differences of the optimum values of ψ_A and ψ_R between the two installation positions are clear.

In conclusion, non-axisymmetric exhausts can also be beneficial for coincident installation positions of UHBR engines. However, the potential of benefit is slightly reduced relative to overlapped configurations. In addition, the installation position changes the optimum placement of both non-axisymmetric exhaust perturbations (ψ_A, ψ_R). For this reason, it is demonstrated that the effects of installation need to be considered in the design of three-dimensional exhaust systems.

E. Effect of the geometry control methods on the design of non-axisymmetric exhausts

The effect of the geometry control methods on the design of non-axisymmetric exhausts is investigated. Two extra datasets of exhaust systems were generated where the differences are the design of the bypass area and after-body (DS3 and DS4) (Table 1, Fig. 7). While dataset DS1 was generated with a uniform $r^{in}_{BP-Exit}$ and a uniform L^{cc}_{TE}, the after-body in DS3 is controlled by the second method (non-uniform L^{cc}_{TE}) and DS4 employs non-circular geometries of the inner annulus of bypass exit (uniform h). Optimisations for maximum ΔNVF are also undertaken with the RSM of datasets DS3 (design DS3-1) and DS4 (design DS4-1). While the optimisation for ΔNVF_{MAX} results in similar ΔNVF for the DS1-1 and DS4-1, DS3-1 is approximately $0.002F_N$ greater ($\Delta NVF = 0.0091F_N$, Fig. 13a). This arises primarily from a greater propulsive force benefit. Therefore, sheared after-bodies that maintain a uniform distribution of β_{cc} are better suited for installed close coupled configurations.

In terms of the non-axisymmetric perturbations of the bypass trailing edge, DS3-1 and DS4-1 also feature inboard shear (Fig 13b). However, both designs have increased ψ_A and reduced θ_A relative to DS1-1. This displacement of the optimum region can also be seen in the performance sensitivity maps (Fig. 14). The radial bump design is similar for DS1-1 and DS3-1, but different for DS4-1 (Fig 13b). In DS4-1 the optimum radius ratio (R/R_{ref}) is at a greater value. In DS4-1 the bypass exit area is controlled with uniform h. This method limits the maximum radius ratio (R/R_{ref}) that

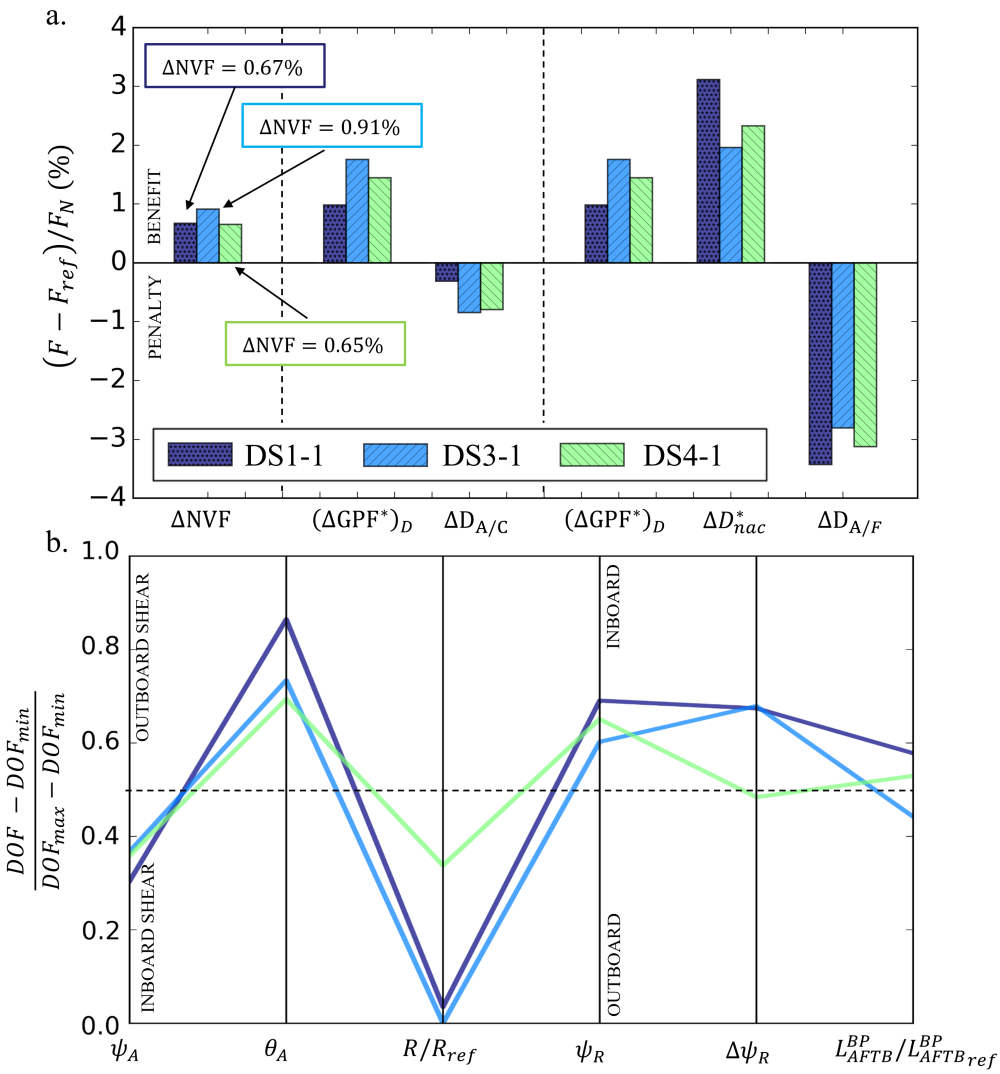

Fig. 13 (a) General decomposition of the net vehicle force benefit and (b) Parallel coordinates chart of designs DS1-1, DS3-1 and DS4-1. Forces are expressed as increments (Δ) relative to the baseline configuration where a positive value implies a beneficial effect. All results are based on RANS CFD assessments.

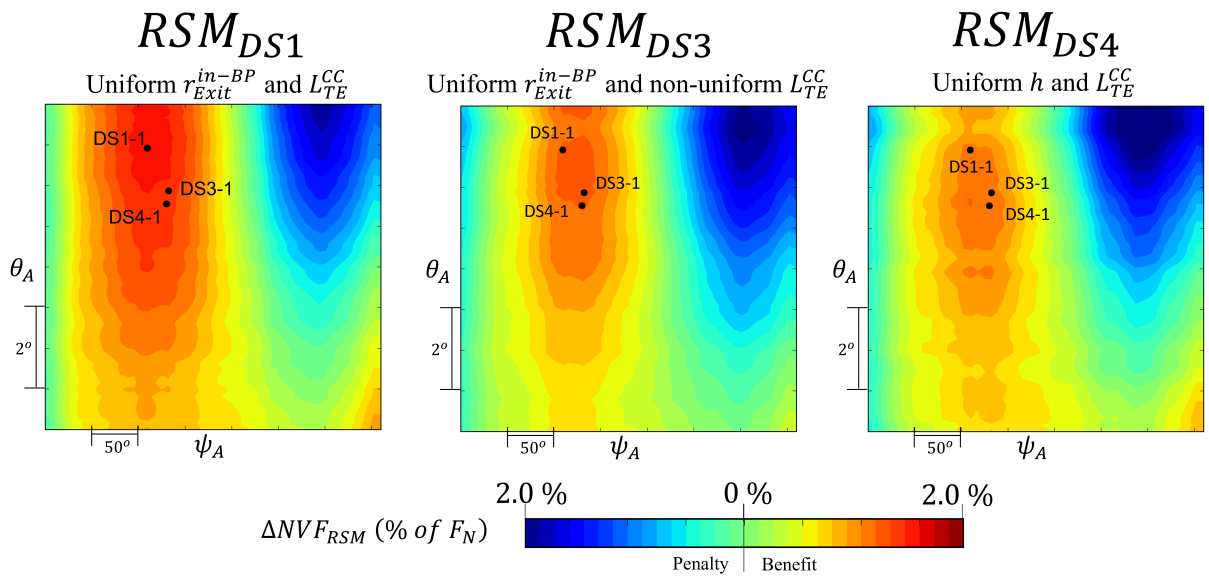

Fig. 14 Design sensitivities of ΔNVF with ψ_A and θ_A for the RSMs constructed with datasets (a) DS1, (b) DS3 and (c) DS4. Each map is obtained perturbing the different RSMs around the optimums. Shaded areas are where the limits on ΔC_d^{BP} and ΔC_d^{CR} are breached.

is beneficial. As the bypass nozzle exit height (h) is kept constant, low values of R/R_{ref} reduce the core cowl boat tail angle and result in an almost flat local region. In conclusion, the different ways of handling the bypass area and after-body lead to different optimum regions of the design space for non-axisymmetric exhausts.

IV. Conclusions

This work presents a low-cost design methodology for installed propulsion systems where a multi-dimensional design space is sampled with a lower-fidelity CFD methodology. The method relies on the acquisition of sufficient data to formulate response surface models at a reduced computational cost relative to the full RANS assessment of the dataset. The optimisation of exhausts for installed UHBR propulsion systems can improve the aircraft net vehicle force by $0.005F_N - 0.009F_N$ when assessed with RANS CFD, depending on the installation position. This is approximately equivalent to a $0.5 - 0.9\%$ reduction in fuel burn. Although the optimisation methodology relies only on RSM constructed with Euler CFD data, it is proven to identify beneficial designs that satisfy the constraints when assessed with RANS.

Exhausts were optimised for different installation positions and with several designs of the bypass area and after-body. It was found that bypass exhausts designed for maximum ΔNVF are sheared towards the inboard side and feature a reduced bypass trailing edge radius, also at the inboard side. The configurations with greater benefits in net vehicle force are designed with circular core cowls (uniform r_{Exit}^{in-BP}) that are sheared at the trailing edge (non-uniform L_{TE}^{cc}). Moreover, non-axisymmetric exhausts have an increased potential of NVF benefit at overlapped configurations (DS1-1, $\Delta NVF = 0.007F_N$) relative to coincident ones (DS2-1, $\Delta NVF = 0.006F_N$).

These findings improve the know-how of the aerodynamic design of civil propulsion systems with non-axisymmetric exhausts, but also enable the exploration and optimisation of complex non-linear systems with an impact on the computational requirements. Moreover, the methodology is fast and flexible and is not restricted to exhaust systems.

Acknowledgments

This work has been partially funded by Rolls Royce plc.

Data availability

Due to commercial confidentiality agreements the supporting data is not available.

References

[1] Brich, N. T., "2020 Vision: The Prospects for Large Civil Aircraft Propulsion," *The Aeronautical Journal*, Vol. 104, No. 1038, 2000, pp. 347–352. doi:10.1017/S0001924000063971.

[2] Berry, D. L., "The Boeing 777 Engine/Aircraft Integration Aerodynamic Design Process," *ICAS Congress 1994, No ICAS-94-6.4.4*, Anaheim, CA, 1994, pp. 1305–1320.

[3] Goulos, I., Otter, J., Tejero, F., Hueso-Rebassa, J., MacManus, D., and Sheaf, C., "Civil turbofan propulsion aerodynamics: Thrust-drag accounting and impact of engine installation position," *Aerospace Science and Technology*, Vol. 111, 2021, p. 106533. doi:10.1016/j.ast.2021.106533.

[4] Otter, J. J., "Aerodynamics and Performance of Civil Aero-Engine Exhaust Systems," PhD Thesis, Cranfield University, Cranfield, Bedfordshire, UK, 2018.

[5] Otter, J. J., Christie, R., Goulos, I., MacManus, D. G., and Grech, N., "Parametric design of non-axisymmetric separate-jet aero-engine exhaust systems," *Aerospace Science and Technology*, Vol. 93, 2019. doi:10.1016/j.ast.2019.05.038.

[6] Otter, J. J., Goulos, I., Christie, R., and MacManus, D. G., "Design and analysis of non-axisymmetric installed aero-engine exhaust systems," *Aerospace Science and Technology*, Vol. 106, 2020. doi:10.1016/j.ast.2020.106210.

[7] Dun, R., "Scarf Nozzle for a jet engine and method of using the same," , 2004. United States Patent, Pub. no. US 2004/0140397 A1.

[8] Munday, D., Mihaescu, M., and Gutmark, E., "Experimental and numerical study of jets from elliptic nozzles with conic plug," *AIAA Journal*, Vol. 49, 2011, pp. 554–564. doi:10.2514/1.J050587.

[9] Kulfan, B., "Recent extensions and applications of the 'CST' universal parametric geometry representation method," *The Aeronautical Journal*, Vol. 114, No. 1153, 2010, p. 157–176. doi:10.1017/S0001924000003614.

[10] Christie, R., Heidebrecht, A., and MacManus, D., "An automated approach to nacelle parameterization using intuitive class shape transformation curves," *Journal of Engineering for Gas Turbines and Power*, Vol. 139, 2017. doi:10.1115/1.4035283.

[11] Christie, R., Robinson, M., Tejero, F., and MacManus, D. G., "The use of hybrid intuitive class shape transformation curves in aerodynamic design," *Aerospace Science and Technology*, Vol. 95, 2019. doi:10.1016/j.ast.2019.105473.

[12] Tejero, F., Goulos, I., MacManus, D., and Sheaf, C., "Effects of Aircraft Integration on Compact Nacelle Aerodynamics," Orlando, Florida, 2020. doi:10.2514/6.2020-2225, aIAA Scitech 2020 Forum, AIAA 2020-2225,1 Part F.

[13] Goulos, I., Stankowski, T., MacManus, D., Woodrow, P., and Sheaf, C., "Civil turbofan engine exhaust aerodynamics: Impact of bypass nozzle after-body design," *Aerospace Science and Technology*, Vol. 73, 2018, pp. 85–95. doi:10.1016/j.ast.2017.09.002.

[14] Goulos, I., MacManus, D., and Sheaf, C., "Civil turbofan engine exhaust aerodynamics: Impact of fan exit flow characteristics," *Aerospace Science and Technology*, Vol. 93, 2019. doi:10.1016/j.ast.2019.05.033.

[15] Skinner, S., and Zare-Behtash, H., "State-of-the-art in aerodynamic shape optimisation methods," *Applied Soft Computing*, Vol. 62, 2018, pp. 933–962. doi:10.1016/j.asoc.2017.09.030.

[16] Kupijai, P., Bestle, D., Flassig, P. M., and Kickenweitz, D., "Automated Multi-Objective Optimization Process for Preliminary Engine Design," *ASME Turboexpo 2012, Volume 1: Aircraft Engine; Ceramics; Coal, Biomass and Alternative Fuels; Controls, Diagnostics and Instrumentation*, American Society of Mechanical Engineers, Copenhagen, Denmark, 2012, pp. 87–96. doi:10.1115/GT2012-68612.

[17] Tejero, F., MacManus, D. G., and Sheaf, C., "Surrogate-based aerodynamic optimisation of compact nacelle aero-engines," *Aerospace Science and Technology*, Vol. 93, 2019. doi:10.1016/j.ast.2019.05.059.

[18] Tejero, F., Christie, R., MacManus, D., and Sheaf, C., "Non-axisymmetric aero-engine nacelle design by surrogate-based methods," *Aerospace Science and Technology*, Vol. 117, 2021. doi:10.1016/j.ast.2021.106890.

[19] Tejero, F., MacManus, D. G., Sanchez-Moreno, F., and Sheaf, C., "Neural network-based multi-point, multi-objective optimisation for transonic applications," *Aerospace Science and Technology*, Vol. 136, 2023, p. 108208. doi:10.1016/j.ast.2023.108208, URL `https://linkinghub.elsevier.com/retrieve/pii/S1270963823001050`.

[20] Goulos, I., Otter, J. J., Stankowski, T., MacManus, D., Grech, N., and Sheaf, C., "Aerodynamic Design of Separate-Jet Exhausts for Future Civil Aero-engines - Part II: Design Space Exploration, Surrogate Modeling, and Optimization," *Journal of Engineering for Gas Turbines and Power*, Vol. 138, 2016. doi:10.1115/1.4032652.

[21] Goulos, I., Otter, J., Stankowski, T., MacManus, D., Grech, N., and Sheaf, C., "Design optimisation of separate-jet exhausts for the next generation of civil aero-engines," *Aeronautical Journal*, Vol. 122, 2018, pp. 1586–1605. doi:10.1017/aer.2018.95.

[22] Forrester, A. I., and Keane, A. J., "Recent advances in surrogate-based optimization," *Progress in Aerospace Sciences*, Vol. 45, 2009, pp. 50–79. doi:10.1016/j.paerosci.2008.11.001.

[23] Krige, D. G., "A statistical approach to some basic mine valuation problems on the Witwatersrand," *Journal of the Southern African Institute of Mining and Metallurgy*, Vol. 52, No. 6, 1951, pp. 119–139.

[24] Smith, S., Nemec, M., and Krist, S., "Integrated Nacelle-Wing Shape Optimization for an Ultra-High Bypass Fanjet Installation on a Single-Aisle Transport Configuration," *51st AIAA Aerospace Sciences Meeting including the New Horizons Forum and Aerospace Exposition, AIAA 2013-0543*, American Institute of Aeronautics and Astronautics, Dallas, Texas, 2013. doi:10.2514/6.2013-543.

[25] Sánchez-Moreno, F., MacManus, D., Hueso-Rebassa, J., Tejero, F., and Sheaf, C., "Optimisation of installed compact and robust nacelles using surrogate models," 2022.

[26] Tejero, F., MacManus, D., Hueso-Rebassa, J., Sanchez-Moreno, F., Goulos, I., and Sheaf, C., "Aerodynamic optimisation of civil aero-engine nacelles by dimensionality reduction and multi-fidelity techniques," *International Journal of Numerical Methods for Heat and Fluid Flow*, 2022. doi:10.1108/HFF-06-2022-0368.

[27] Tejero, F., MacManus, D., and Sheaf, C., "Impact of Droop and Scarf on the Aerodynamic Performance of Compact Aero-Engine Nacelles," 2020. doi:10.2514/6.2020-1522, AIAA Scitech 2020 Forum, AIAA-1522.

[28] Levy, D. W., Laflin, K. R., Tinoco, E. N., Vassberg, J. C., Mani, M., Rider, B., Rumsey, C. L., Wahls, R. A., Morrison, J. H., Brodersen, O. P., Crippa, S., Mavriplis, D. J., and Murayama, M., "Summary of Data from the Fifth Computational Fluid Dynamics Drag Prediction Workshop," *Journal of Aircraft*, Vol. 51, 2014, pp. 1194–1213. doi:10.2514/1.C032389.

[29] Vassberg, J. C., Tinoco, E. N., Mani, M., Rider, B., Zickuhr, T., Levy, D. W., Brodersen, O. P., Eisfeld, B., Crippa, S., Wahls, R. A., Morrison, J. H., Mavriplis, D. J., and Murayama, M., "Summary of the Fourth AIAA Computational Fluid Dynamics Drag Prediction Workshop," *Journal of Aircraft*, Vol. 51, 2014, pp. 1070–1089. doi:10.2514/1.C032418.

[30] Rivers, M., and Dittberner, A., "Experimental Investigations of the NASA Common Research Model in the NASA Langley National Transonic Facility and NASA Ames 11-Ft Transonic Wind Tunnel (Invited)," *49th AIAA Aerospace Sciences Meeting including the New Horizons Forum and Aerospace Exposition, AIAA 2011-1126*, American Institute of Aeronautics and Astronautics, Orlando, Florida, 2011. doi:10.2514/6.2011-1126.

[31] Rivers, M. B., and Dittberner, A., "Experimental Investigations of the NASA Common Research Model," *Journal of Aircraft*, Vol. 51, 2014, pp. 1183–1193. doi:10.2514/1.C032626.

[32] ISO International Standard 2533-1975, "Standard Atmosphere First Edition," Tech. rep., ISO, Geneva, Switzerland, 1978.

[33] Goulos, I., Stankowski, T., Otter, J., MacManus, D., Grech, N., and Sheaf, C., "Aerodynamic Design of Separate-Jet Exhausts for Future Civil Aero-engines - Part I: Parametric Geometry Definition and Computational Fluid Dynamics Approach," *Journal of Engineering for Gas Turbines and Power*, Vol. 138, 2016. doi:10.1115/1.4032649.

[34] Hueso-Rebassa, J., Tejero, F., Otter, J., Goulos, I., and MacManus, D., "Multi-Fidelity Assessment of Exhaust Systems for Complete Engine-Aircraft Configurations," *Proceedings of Aerospace Europe Conference 2020 (AEC2020), 00337*, Bordeaux, France, 2020.

[35] Ansys Inc, "ANSYS FLUENT User's Guide," Tech. rep., 2021.

[36] Menter, F. R., "Two-Equation Eddy-Viscosity Turbulence Models for Engineering Applications," *AIAA Journal*, Vol. 32, No. 8, 1994, pp. 1598–1605.

[37] Sutherland, W., "The Viscosity of Gases and Molecular Force," *Philosophical Magazine Series 5*, Vol. 36, 1893, pp. 507–531.

[38] Mikkelsen, K. L., Myren, D. J., Dahl, D. G., and Christiansen, M., "Initial Subscale Performance Measurements of the AIAA Dual Separate Flow Reference (DSFR) Nozzle," *AIAA Propulsion and Energy Forum, 51st AIAA/SAE/ASEE Joint Propulsion Conference, AIAA2015-3883*, American Institute of Aeronautics and Astronautics, Orlando, Florida, 2015. doi:10.2514/6.2015-3883.

[39] AGARD, "Aerodynamics of Power Plant Installation," Tech. rep., 1981.

[40] Olsson, A., Sandberg, G., and Dahlblom, O., "On Latin hypercube sampling for structural reliability analysis," *Structural Safety*, Vol. 25, 2003, pp. 47–68. doi:10.1016/S0167-4730(02)00039-5.

[41] Tonda, A., "Inspyred: Bio-inspired algorithms in Python," *Genetic Programming and Evolvable Machines*, Vol. 21, 2020, pp. 269–272. doi:10.1007/s10710-019-09367-z.

[42] Kohavi, R., "A Study of Cross-Validation and Bootstrap for Accuracy Estimation and Model Selection," *Proceedings of the 14th International Joint Conference on Artificial Intelligence - Volume 2*, Morgan Kaufmann Publishers Inc., San Francisco, CA, USA, 1995, p. 1137–1143.

[43] Hueso-Rebassa, J., "Design, Performance and Aerodynamics of Non-Axisymmetric Exhaust Systems for Civil Aero-Engines," PhD Thesis, Cranfield University, Cranfield, Bedfordshire, UK, 2022.

2023-06-08

Design considerations of non-axisymmetric exhausts for large civil aero-engines

Hueso Rebassa, Josep

AIAA

Hueso-Rebassa J, MacManus DG, Goulos I, Tejero F. (2023) Design considerations of non-axisymmetric exhausts for large civil aero-engines. In: 2023 AIAA Aviation and Aeronautics Forum and Exposition (AIAA AVIATION Forum), 12-16 June 2023, San Diego, CA

https://doi.org/10.2514/6.2023-3467